



Thermography analysis and porosity formation during laser beam welding of AA5083-H111 aluminum alloy

Mustafa Umar¹ · Sathiya Paulraj¹

Received: 4 March 2020 / Accepted: 28 July 2020 / Published online: 10 August 2020
© Akadémiai Kiadó, Budapest, Hungary 2020

Abstract

In this work, the thermal characteristics of the weld pool during Yb:YAG laser welding of the AA5083-H111 aluminum alloy were captured using an infrared thermal imaging camera and a numerical model was developed to predict the temperature fields using COMSOL Multiphysics software. On comparing the measured and predicted temperature of the weld pool surface, the deviation was below 10 °C and the average experimental error was not more than 1%. It shows the reliability of IR camera used in this investigation. Also, it was apparent from the thermal images that at a higher beam power, an erratic molten pool was created due to the instability of keyhole and spatters were ejected from the molten pool. The higher recoil pressure built at the walls of keyhole due to the high intensity of the laser beam and instigation of the ejected fluid flow mechanism was responsible for this occurrence. Also, the formation and floating mechanisms of process-induced porosities were analyzed. Porosities were identified in the weldments processed with longer shielding gas blown distance (30 mm), whereas other welds had no porosities. Since the gas blown distance was more, gas pressure over the molten pool was not sufficient to suppress the plasma plume and, thereby, results in porosity formation. Interestingly, a high number of porosities were evident at the toe of the weld bead and it was assumed to be caused by the high thermal gradient-induced Marangoni flow. This study provides a better understanding of molten pool behavior, porosity formation and its floating mechanism.

Keywords Aluminum alloy · Laser welding · Thermography · Simulation · Porosity

Introduction

The AA5083 aluminum alloys are extensively used in marine, aerospace and automobile industries due to their significant characteristics such as excellent strength, corrosion resistance, formability and weldability. Laser beam welding (LBW) is an advanced manufacturing process which is widely used in the industries for joining materials because of its specific advantages such as higher depth-to-width ratio, narrow heat-affected zone (HAZ), faster travel speed and easy for automation [1, 2]. During LBW, the high-energy beam hits the metal surface and evaporates the material in that region which forms the keyhole rapidly and the combined effect of complex multiphase fluid flow and unstable keyhole procedure on the weld bead. Moreover, the high-energy-density beam enables the heat source to focus more

on a small spot and allows the weld pool to become narrower and deeper [3–5]. Since the thermal characteristics of aluminum alloys significantly influence the joint properties, to monitor and control the fluid flow behavior during LBW, various techniques such as coaxial monitoring system and high-speed cameras have been used in many instances [6–8]. However, thermography is a convenient way of measuring temperature fields. The measurements can be used to calibrate the results of the simulation and to study the information on thermal phenomena that occur during welding. The application of non-contact infrared (IR) thermal imaging camera is limited due to the high reflectivity of the metal surface and higher wavelength of laser beam [9]. If the material is highly reflective, the reflected laser beam that comes from the metal surface could damage the optics such as lens and filters of the IR camera. Hence, proper care must be taken to avoid reflection-related issues [10, 11].

Another problem associated with LBW of aluminum 5083 alloy is porosity, and the instability of keyhole causes it during full penetration welding [12, 13]. The keyhole-induced porosity formation is one of the two major

✉ Sathiya Paulraj
psathiya@nitt.edu

¹ Department of Production Engineering, National Institute of Technology, Tiruchirappalli, Tamilnadu 620015, India

Table 1 Elemental compositions of the base alloy (mass%)

Elements	Cu	Si	Fe	Mg	Mn	Cr	Ni	Ti	Zn	Al
AA5083-H111	0.02	0.12	0.4	4.57	0.94	0.06	0.01	0.027	0.02	Bal.

mechanisms associated with aluminum welding. The other mechanism is instigated by the low-boiling-point elements such as magnesium and hydrogen in Al–Mg alloys. The shape of these porosities is perfectly spherical and often seen in aluminum weldments if the amount of hydrogen is not controlled [14–17]. Large-sized porosity leads to cracking even though it is irregular in shape and reduces the strength of the welds. However, the number of porosities formed during LBW can be reduced by performing surface preparation techniques such as sandblasting and emery polishing before welding. Also, the use of dual-beam laser welding can be adequate for reducing porosity formation in weldments [18, 25].

Though a wide range of experiments have been conducted on predicting thermal fields, fluid flow and porosity formation using simulation techniques, there is still a need to focus on real-time monitoring of the weld pool with IR thermal imaging camera. Hence, in this work, an Optris PI 1M model thermal imaging camera was used to capture the thermal information during Yb:YAG LBW of 3-mm-thick AA5083-H111 aluminum alloy. Also, the temperature fields were predicted using COMSOL 5.3a Multiphysics software, and the data were compared with the experimental results. Also, the influence of process parameters on porosity formation and its floating mechanism has been studied.

Materials and methods

LBW of aluminum 5083 alloy

The 3-mm-thick AA5083-H111 alloy was used for this investigation due to its extensive industrial usage and susceptibility to porosity during welding. The elemental compositions of primary alloying elements existing in the base alloy are given in Table 1. Before welding, the oxide layer was removed mechanically and the abutting edges were cleaned with acetone. The butt joints were made using a six-axis robotized Yb:YAG laser welding machine which has the maximum beam power of 4 kW. The laser beam had a wavelength of 1030 nm, and the focal spot size was 0.2 mm. 99.99% pure argon was used as a shielding gas, and the flow rate was kept constant at 20 lpm. Factors and their levels were chosen for this work shown in Table 2. An L9-Taguchi design was adopted to carry out the experiments based on the scheme shown in Table 3.

Table 2 Laser welding process parameters and their ranges

Factors/levels	Level I	Level II	Level III
Power (P)/kW	1.5	2	2.5
Welding speed (V)/mm min ⁻¹	200	300	400
Shielding gas blown distance (D)/mm	10	20	30
Focal length (F)/mm	–3	0	3

Table 3 Taguchi design-based L9 orthogonal array

Exp. no.	P /kW	V /mm min ⁻¹	D /mm	F /mm
1	1.5	200	10	–3
2	1.5	300	20	0
3	1.5	400	30	3
4	2	200	20	3
5	2	300	30	–3
6	2	400	10	0
7	2.5	200	30	0
8	2.5	300	10	3
9	2.5	400	20	–3

Thermography

An Optris PI 1M model IR thermal imaging camera was used for capturing thermal information of weld pool surface. The IR camera has a short measurement wavelength of 1 μ m, and the reaction time of high-performance electronic sensor is 1 ms to show the temperature information of the center pixel. Also, it has full measurement ranges from 450 to 1800 °C. The camera was interfaced with a computer to monitor the molten pool in real time, and the same was recorded for further analysis. The camera was positioned slightly angular to the weld line (as shown in Fig. 1) to avoid detrimental effects of the reflective beam that comes from the metal surface [26].

Numerical simulation modeling

To determine the thermal fields on the weld pool surface, a numerical simulation was carried out using COMSOL 5.3a Multiphysics software. Several thermophysical properties of 5083 aluminum alloy and related parameters considered for this work are presented in Table 4.

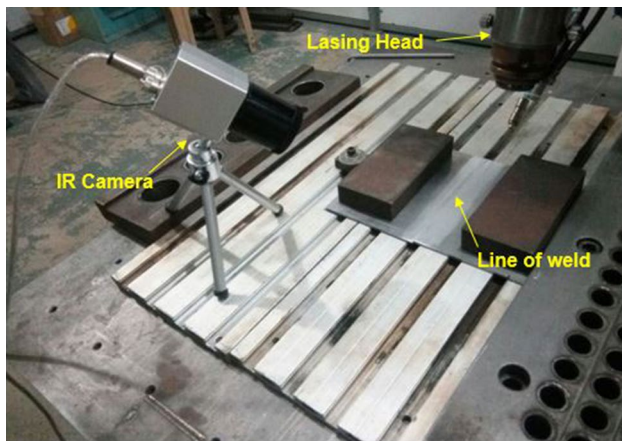


Fig. 1 Laser welding setup and arrangement of IR camera

Assumptions

Some assumptions made to construct the mathematical model are as follows [9–16]: (1) The molten metal is assumed to be a Newtonian fluid, is laminar and is incompressible. (2) The heat source is modeled as a Gaussian density distribution. (3) The effects of shielding gas and its rate of flow on molten metal are omitted. (4) Physical properties of the molten and solid metal are kept as constant. (5) The internal heat flux is often a sum of the contributions from various heat transfer processes such as conduction, convection and radiation. If $Q=0$, the particular case arises, called as thermal insulation.

Laser heat source model

To simulate the thermal distribution, a three-dimensional moving heat source is modeled and it is expected to be a Gaussian heat flux distribution model on the weld pool as shown in Fig. 2. It has been proven that [9–18] the Gaussian heat flux distribution is the best suitable one for simulating moving heat source, and the heat flux can be calculated using the following formula:

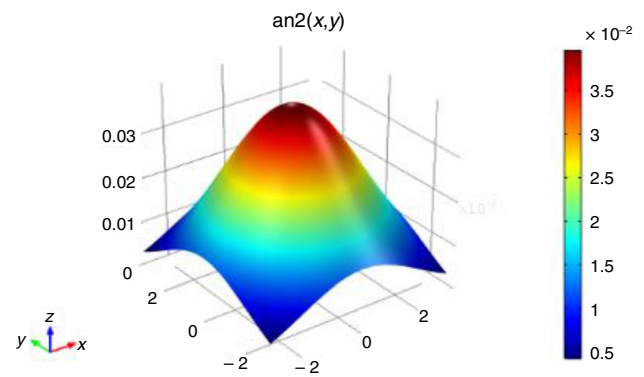


Fig. 2 Gaussian heat distribution model

$$Q = Q_0 \frac{e^{-\frac{(x^2+y^2)}{2*\sigma^2}}}{2 * \pi * \sigma^2} \tag{1}$$

where σ is the radial distance; in this case, $\sigma = (X - X_0)^2 + (Y - Y_0)^2$ where (X_0, Y_0) is the origin and X, Y denotes the linear distances from the origin as shown in Fig. 2.

The parameters used for the numerical simulation are given in Tables 3 and 4. The 3D model of the 5083 alloy sheets was discretized into finite element mesh using tetrahedral elements. As the heat source is introduced at the butting ends of the sheets, a finer mesh was created along the butted edges using smaller-sized elements and the other regions were meshed by coarser elements. The finite element mesh of the model is shown in Fig. 3. The cut plane shown in Fig. 3 was defined at a distance of 100 mm from the origin in the direction of the y-axis to get the shape of the weld bead which is time dependent. A 3D point was also defined at the same location to detect the temperature variation concerning time.

Governing equations

Governing equations indicate the state of a system and are used for analyzing the computation of temperature

Table 4 The thermophysical properties of AA5083 aluminum alloy

Nomenclature	Value	Nomenclature	Value
Density (l)	2380/kg m ⁻³	Density (s)	2660/kg m ⁻³
Viscosity	4.2 × 10 ⁻³ /kg m ⁻¹ s ⁻¹	Liquids temperature	933/K
Solidus temperature	847/K	Heat transfer coefficient	20/W m ⁻² K ⁻¹
Specific heat (l)	1197.21/J kg ⁻¹ K ⁻¹	Specific heat (s)	1050/J kg ⁻¹ K ⁻¹
Surface tension	0.871 N m ⁻¹	Surface tension gradient	-0.000155/N m ⁻¹ K ⁻¹
Latent heat of fusion	3.87 × 10 ⁵ /J kg ⁻¹	Thermal conductivity (s)	235 W/m ⁻¹ K ⁻¹
Thermal conductivity (l)	90/W m ⁻¹ K ⁻¹	Coefficient of thermal expansion	1.5 × 10 ⁻⁴ /K ⁻¹

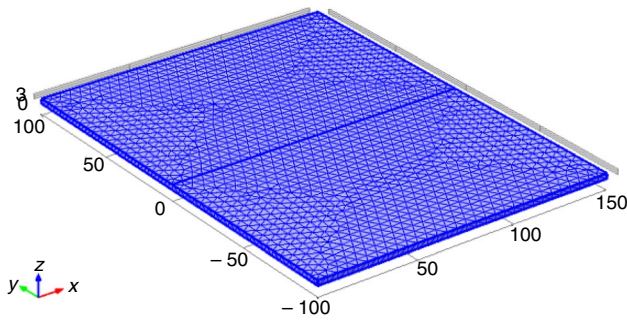


Fig. 3 Finite element mesh model

distribution. The heat transfer equations used to determine the thermal characteristics are given as follows [10]:

For calculating the thermal cycles:

$$\frac{\partial^2 T}{\partial x^2} + \frac{\partial^2 T}{\partial y^2} + \frac{\partial^2 T}{\partial z^2} + \frac{q_g}{k} = \rho c_p \frac{\partial T}{\partial t} \quad (2)$$

For calculating the conductive, convective and radiative heat losses [5]:

$$q'' = k \nabla T \quad (3)$$

$$q'' = h(T_{\text{sur}} - T_{\text{amb}}) \quad (4)$$

$$q'' = \epsilon \sigma (T_{\text{amb}}^4 - T^4) \quad (5)$$

where ρ is the density, k is the thermal conductivity, C_p is the specific heat capacity at constant pressure, q_g is the internal heat generation per volume, t is the time and T is the temperature of the surface along the (xyz) coordinates. Also, q'' is the heat flux flowing in that direction, T_{amb} is the ambient temperature, T_{sur} is the surface temperature and h is the heat transfer coefficient. In Eq. (5), σ denotes the Stefan–Boltzmann constant and ϵ denotes the emissivity. The emissivity is taken as 0.15 for all the surfaces radiating to the environment.

The essential boundary condition (EBC) and natural boundary condition (NBC) considered for solving the governing equations are as follows:

$$T_{\text{amb}} = 20 \text{ }^\circ\text{C} \text{ for EBC,}$$

$$q'' = \text{power as influx heat for NBC.}$$

Results and discussion

Thermal characteristics of the weld pool

During LBW of materials, many mechanisms are taking place in the molten pool. At the initial stage, the high-energy-density laser beam focusing on a tiny spot melts and evaporates the metal surface to form a keyhole. The evaporation process becomes more intense in the molten pool by absorbing more beam energy which induces rapid heating and then solidifies to form the weld bead [6–14]. The structural characteristics and performance of the joints are highly related to their weld geometry. Since the weld geometry had a great impact on the thermal properties of the material and fluid flow, it is important to understand the mechanisms arising during LBW [1]. Here, the thermal characteristics of the weld pool created during LBW of 5083 aluminum alloy were captured using IR thermal imaging camera, and the illustrations are shown in Fig. 4a–i. In Fig. 4a–i, the reflections of the laser beam, gas nozzle tip and lasing head are visible due to the reflectiveness of the metal surface. Since the aluminum has a highly reflective surface, a part of beam energy was dissipated to the atmosphere through reflections which led to partial absorption and resulted in incomplete penetration. The amount of beam absorbed by the metal surface can be increased through increasing surface roughness [19–23].

There was no trace of solidification line behind the molten pool, and it confirms the rapid solidification mechanism which is obvious in LBW process. Also, it is evident from Fig. 4a–c that the shape of the molten pool has changed with varying welding speeds and focal lengths for a constant beam power (1.5 kW). An increase in laser beam power to 2 kW increased the fluidity and created an inconsistent molten pool as shown in Fig. 4d–f. Further increasing the beam power to 2.5 kW created an erratic molten pool which ejected molten aluminum from the weld pool as spatters. Figure 4g–i shows the expulsion of molten metal, and the fluid flow in the weld pool was responsible for the formation of spatters [15–18]. There are two major fluid flows involved in the molten pool: One is surface fluid flow and the other is ejected fluid flow. In surface fluid flow, the surface and inner molten metal were driven by the buoyancy forces, whereas in ejected fluid flow, the molten metal was driven by the recoil pressure from the bottom to the top surface of the weld pool [5]. Hence, the increase in beam intensity at

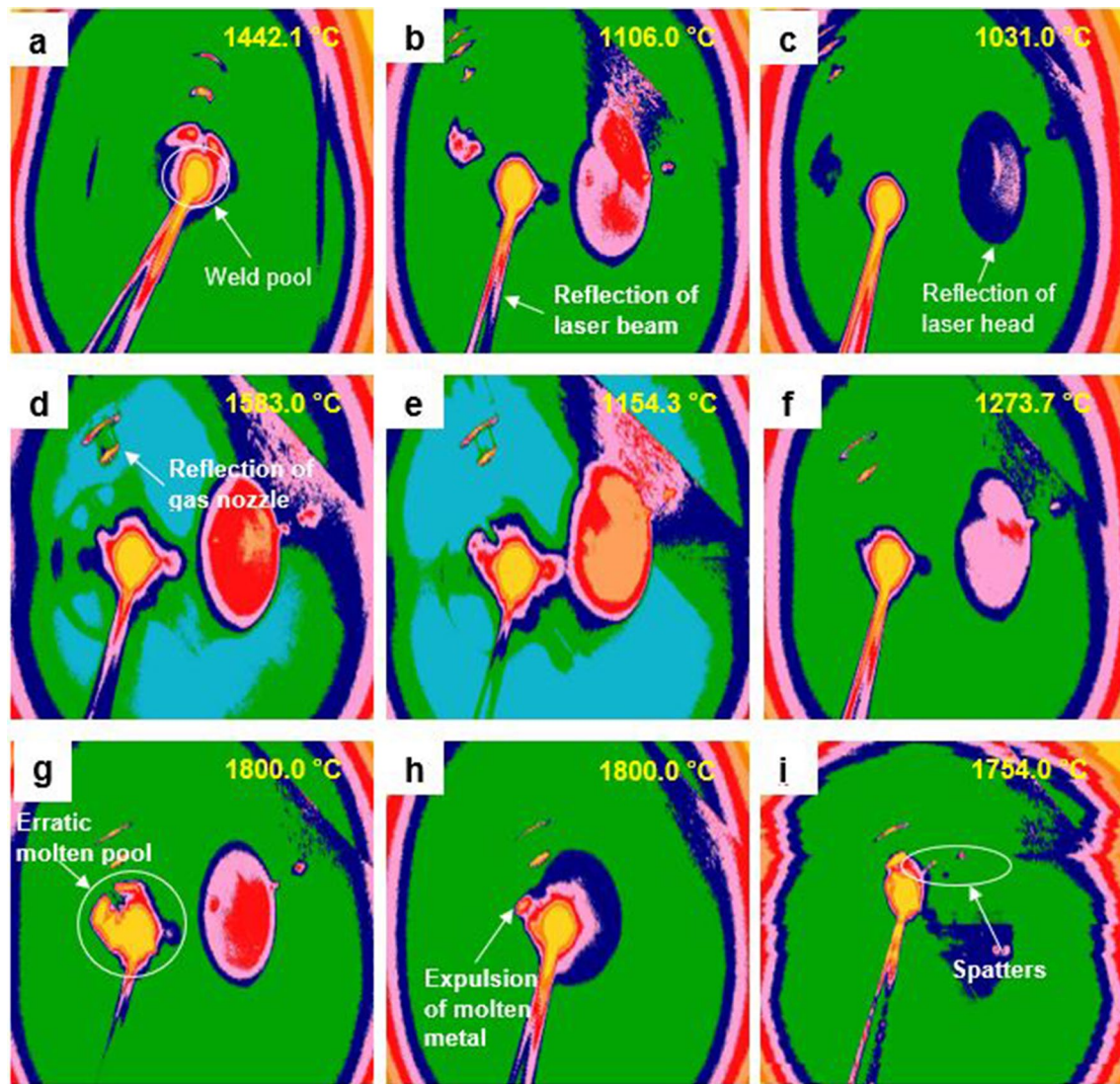


Fig. 4 Thermal images showing the shape and temperature information of weld pool: **a** Exp.1; **b** Exp.2; **c** Exp. 3; **d** Exp. 4; **e** Exp. 5; **f** Exp.6; **g** Exp.7; **h** Exp. 8; **i** Exp. 9

a higher level increased the recoil pressure at the walls of keyhole, and it could be the reason for spatter formation [15, 16, 18, 23].

Model validation

To validate the observed weld pool temperature, a finite element model was constructed and developed for all the parameters shown in Table 3. The simulated results for the welding conditions ($P=2.5$ kW, $V=300$ mm min^{-1} , $F=3$ mm) are presented in Fig. 5a–d. The simulated values agree well with experimental results, and the temperature of simulated weld pools was also very close to the values obtained by IR thermal camera.

Comparison of experimental results with simulated weld pool temperature

Further, to verify the performance of IR thermal imaging camera, the experimental results have been compared with simulated results. The predicted maximum temperature with measured thermal fields (Fig. 4) is presented in Table 5.

Figure 6 clearly shows that the predicted temperature results of the established simulation model had a good association with the experimental outcomes. From Fig. 6 and Table 5, it is apparent that except experiments 7 and 8, the deviation between predicted and the measured value was less than 10 °C and the average experimental error was less than 1%. It shows the reliability of the IR camera used in this investigation. In the case of experiments 7 and 8,

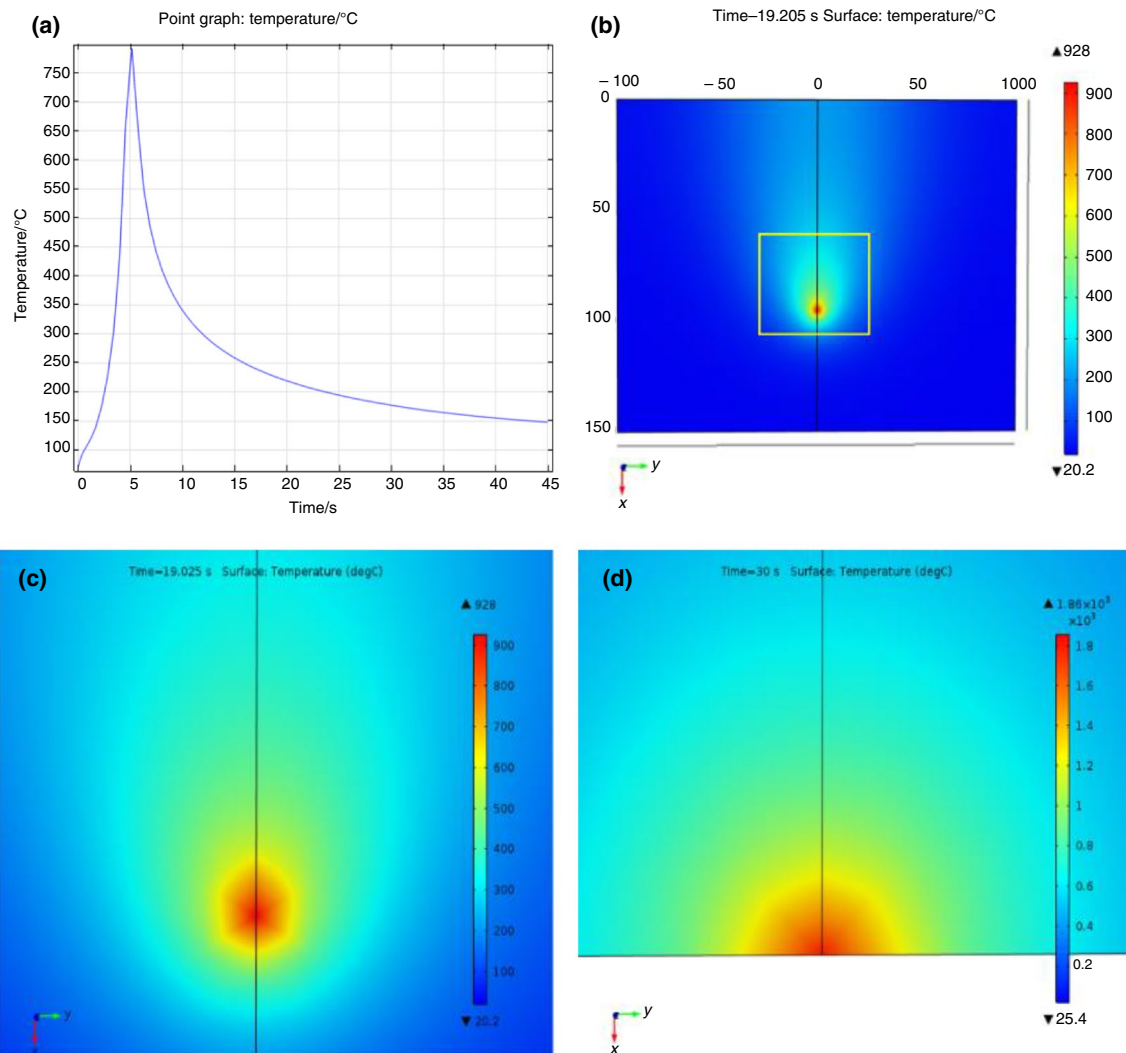


Fig. 5 Simulation results of experiment 8 showing shape and temperature information of weld pool: **a** at $t=5$ s; **b** at $t=19.025$ s; **c** framed portion in **(b)**; **d** at $t=30$ s (max. temp.)

the predicted value was exceeded the maximum measuring capacity (1800 °C) of the IR camera used. Therefore, a higher order of deviation occurred. Also, the shielding gas and plasma effects on the molten pool surface could be one of the reasons behind experimental deviations.

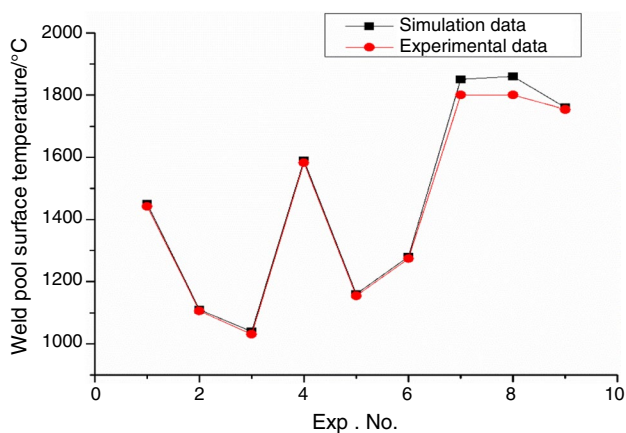
Porosity formation during LBW

The periodic collapse of the keyhole and unstable fluid flow in the weld pool are the contributors of porosity. At

a higher energy density, the flow behavior of molten metal is expected to become unstable and to induce recirculation which forms the process-induced porosities [5]. The process-induced porosity is one of the main mechanisms involved in bubble formation. To understand the bubble or porosity formation mechanism experimentally, the weld beads made for the process conditions given in Table 3 were cut and the cross section of weld beads was studied under a microscope shown in Fig. 7a–i. From Fig. 7a–i, it is apparent that not all the weld beads have a bubble or porosity in them.

Table 5 The maximum temperature at the weld pool: predicted and measured

Exp. no.	Maximum temperature/°C			Experimental error/%
	Predicted	Measured	Exp. deviation	
1	1450	1442.1	7.9	0.54
2	1110	1106	4.0	0.36
3	1040	1031	9.0	0.87
4	1590	1583	7.0	0.44
5	1160	1154.3	5.7	0.49
6	1280	1273.7	6.3	0.49
7	1850	1800	50	2.7
8	1860	1800	60	3.3
9	1760	1754	6.0	0.34

**Fig. 6** Comparison of the predicted and measured temperature

The shielding gas parameters such as flow rate, blowing angle and blowing distance were reported to have a great influence in the formation of porosity [7]. A proper flow rate could suppress the plasma plume in the keyhole, and decreasing blown angle to 30° reduced the number of pores [17, 24]. As the gas flow rate and blown angle were kept constant in this work, the blown distance alone showed a great impact on porosity formation. Irrespective of other parameters, only the weld beads processed with longer shielding gas blown distance (30 mm) have porosities in the microstructure, which is shown in Fig. 7c, e, g. The bubble was formed at the bottom of the keyhole and stayed in without getting collapsed. The plasma plume over the molten surface was not suppressed due to insufficient gas pressure. Since the distance between the gas nozzle and the molten pool was more (30 mm), the shielding gas effects on the molten pool were minimized. Interestingly, in Fig. 7e, the porosities are observed at the toe of weld bead, which is not evident in other beads. The formed bubbles were floated along the sidewall of molten pool (as indicated by red arrow in Fig. 7e) and trapped at the toe of the bead. This phenomenon is caused by the recirculation flow of molten pool at the front wall. Also, it is believed that the high thermal gradient-induced Marangoni flow is responsible for the recirculation at the melting front [5, 13]. However, the thickness of the material also has some effect on porosity formation. As the heat source passes rapidly, the time taken by any vapor or gas formed to travel through the thickness could be insufficient [7]. From the results, it is obvious that this investigation provides more insights to have a better understanding of various porosity formation mechanisms involved in laser welding.

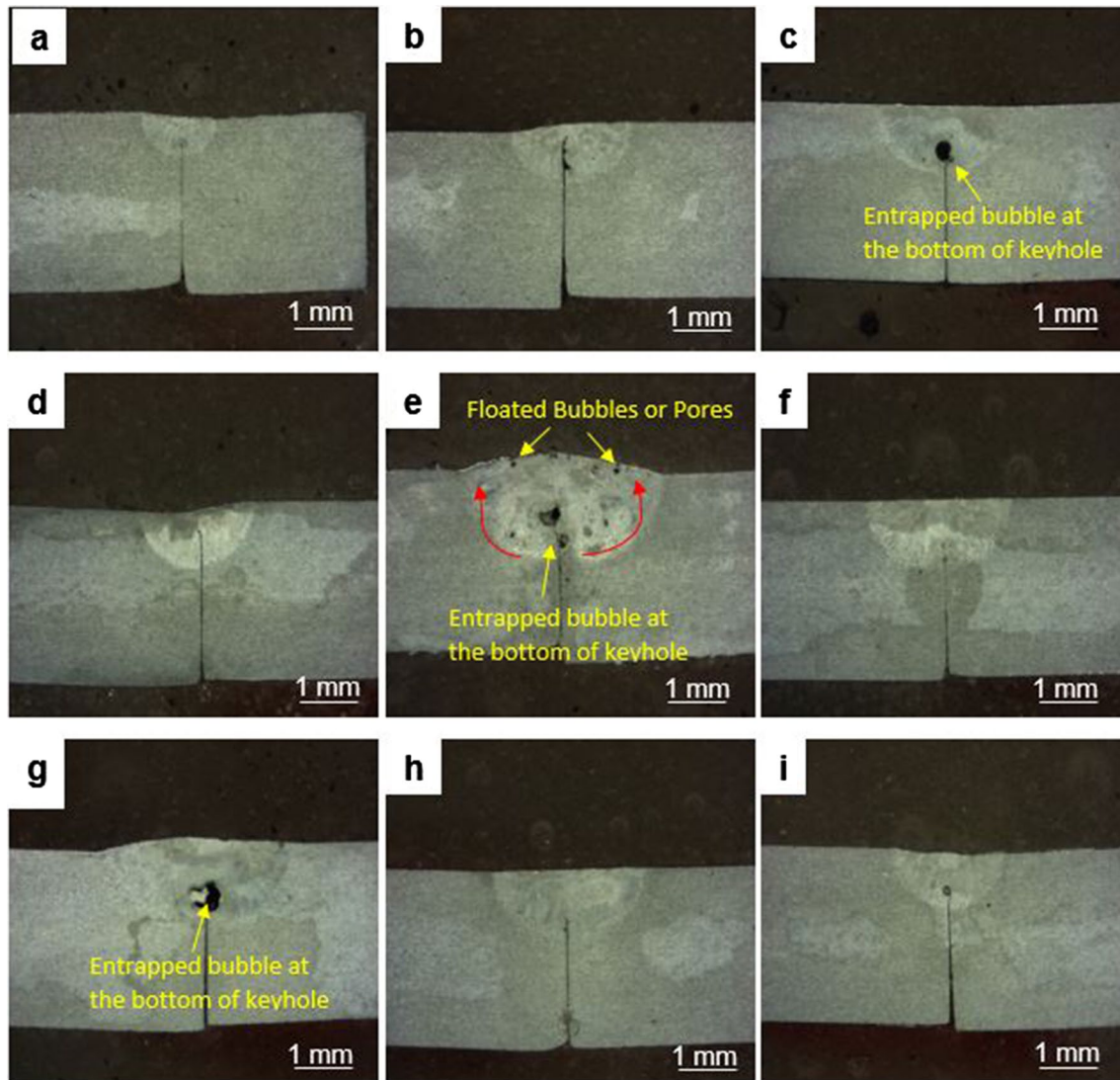


Fig. 7 Macrostructure of weld beads: **a** Exp.1; **b** Exp.2; **c** Exp. 3; **d** Exp. 4; **e** Exp. 5; **f** Exp.6; **g** Exp.7; **h** Exp. 8; **i** Exp. 9

Conclusions

The thermal characteristics of weld pool during Yb:YAG laser beam welding of the AA5083-H111 aluminum alloy were captured using an infrared thermal imaging camera, and the results were compared with simulation data. Also, the experimental results were discussed to deepen the understanding of porosity formation and its floating mechanisms. The following conclusions were drawn from this study:

- The predicted data of the established simulation model had a good association with the experimental results, and the proposed model can be utilized to understand the thermal characteristics of weld pool.
- It is apparent that except experiments 7 and 8, the deviation between predicted and measured temperature was less than 10 °C and the average experimental error was less than 1%. Hence, it indicates that the IR camera used in this investigation was reliable and it can be used for collecting thermal information of molten metal.
- Thermal images show that the shape of the molten pool keeps changing with a change in welding speed and focal length for a constant beam power.
- At a higher beam power, an erratic molten pool was created due to the change in fluid flow and spatters were ejected from molten pool. The recoil pressure built at the walls of keyhole due to the high intensity of laser beam and instigation of ejected fluid flow mechanism was observed to be responsible for this occurrence.

- Irrespective of other parameters, the shielding gas blown distance alone showed a great impact on porosity formation. Porosities were identified in the weldments processed with longer shielding gas blown distance (30 mm), whereas there was no evidence of porosities in other welds.
- A higher number of porosities were evident at the toe of weld bead, and it was assumed to be caused by longer shielding gas blown distance which encouraged the high thermal gradient-induced Marangoni flow, resulting in recirculation flow of molten pool at the front wall.

Acknowledgements The authors would like to express their most profound appreciation and sincere thanks to the Department of Science and Technology—Science and Engineering Research Board (DST-SERB), New Delhi, India, for financially supporting this entire research work, under the sponsored research project sanctioned no. SB/EMEQ-168/2014, dated 29-01-2016.

References

1. Yuewei A, Ping J, Xinyu S, Peigen L, Chunming W. A three-dimensional numerical simulation model for weld characteristics analysis in fiber laser keyhole welding. *Int J Heat Mass Transf.* 2017;108:614–26.
2. Lijin H, Dongsheng W, Xueming H, Shichao L, Zhao J, Fang L, Huan W, Shaojian S. Effect of the welding direction on the microstructural characterization in fiber laser-GMAW hybrid welding of 5083 aluminum alloy. *J Manuf Process.* 2018;31:514–22.
3. Dabin Z, Canli L, Xixia L, Yang C, Dongsheng W. Numerical study of spatter formation during fiber laser welding of aluminum alloy. *J Manuf Process.* 2018;31:72–9.
4. Sanchez A, Delgado T, Gonza L, Botana FJ. Laser welding of aluminium alloys 5083 and 6082 under conduction regime. *Appl Surf Sci.* 2009;255:9512–21.
5. Chinnapat P, Bama P, Mark W, Nathanael T, Richard P, Jeffery B, Hector C. Keyhole formation and thermal fluid flow-induced porosity during laser fusion welding in titanium alloys: experimental and modelling. *Acta Mater.* 2017;126:251–63.
6. Masiyang L, Yung CS. Vision-based weld pool boundary extraction and width measurement during keyhole fiber laser welding. *Opt Lasers Eng.* 2015;64:59–70.
7. Kai L, Fenggui L, Haichao C, Xibin L, Xinhua T, Zhuguo L. Investigation on the effects of shielding gas on porosity in fiber laser welding of T-joint steels. *Int J Adv Manuf Technol.* 2015;77:1881–8.
8. Baohua C, Jon B, Chris A, Paul H. Studies on the spatter behaviour when welding AA5083 with a Yb-fibre laser. *Int J Adv Manuf Technol.* 2016;84:1769–76.
9. Simone M, Dominique G, Alexandre M, Laetitia K. Using infrared thermography in order to compare laser and hybrid (laser + MIG) welding processes. *Opt Laser Technol.* 2009;41:665–70.
10. Maryna S, Simone M, Michel P, Mariana I. The infrared thermography control of the laser welding of amorphous polymers. *NDT & E Int.* 2008;41:178–83.
11. Huang RS, Liu LM, Song G. Infrared temperature measurement and interference analysis of magnesium alloys in hybrid laser-TIG welding process. *Mater Sci Eng A.* 2007;447:239–43.
12. Tsirkas SA, Papanikos P, Kermanidis TH. Numerical simulation of the laser welding process in butt-joint specimens. *J Mater Process Technol.* 2003;134:59–69.
13. Runqi L, Hui W, Fenggui L, Joshua S, Blair C. Numerical study of keyhole dynamics and keyhole-induced porosity formation in remote laser welding of Al alloys. *Int J Heat Mass Transf.* 2017;108:244–56.
14. Matsunawa A, Mizutani M, Katayama S, Seto N. Porosity formation mechanism and its prevention in laser welding. *Weld Int.* 2003;17(6):431–7.
15. Dongsheng W, Xueming H, Lijin H, Jiang Z. Numerical simulation of spatter formation during fiber laser welding of 5083 aluminum alloy at full penetration condition. *Opt Laser Technol.* 2018;100:157–64.
16. Dongsheng W, Xueming H, Fang L, Lijin H. Understanding of spatter formation in fiber laser welding of 5083 aluminum alloy. *Int J Heat Mass Transf.* 2017;113:730–40.
17. Haboudou A, Peyre P, Vannes AB, Peix G. Reduction of porosity content generated during Nd:YAG laser welding of A356 and AA5083 aluminium alloys. *Mater Sci Eng A.* 2003;363:40–52.
18. Sanchez A, Delgado T, Damborenea JJ, Lopez V, Botana FJ. Laser welding of AA 5083 samples by high power diode laser. *Sci Technol Weld Join.* 2009;14(1):78–86.
19. Marcin K, Wiesława P, Sebastian S. Modelling of laser beam heat source based on experimental research of Yb:YAG laser power distribution. *Int J Heat Mass Transf.* 2015;83:679–89.
20. Tsirkas SA. Numerical simulation of the laser welding process for the prediction of temperature distribution on welded aluminium aircraft components. *Opt Laser Technol.* 2018;100:45–56.
21. Hamidreza H, Homam NM. Hot cracking in pulsed Nd:YAG laser welding of AA5456. *Opt Laser Technol.* 2018;103:22–32.
22. Lei W, Yanhong W, Jicheng C, Wenyong Z. Macro-micro modeling and simulation on columnar grains growth in the laser welding pool of aluminum alloy. *Int J Heat Mass Transf.* 2018;123:826–38.
23. Lijin H, Xueming H, Dongsheng W, Li F, Yan C, Youxiong Y. Effect of magnesium content on keyhole-induced porosity formation and distribution in aluminum alloys laser welding. *J Manuf Process.* 2018;33:43–53.
24. Kakitani R, de Gouveia GL, Garcia A, Cheung N, Spinelli J. Thermal analysis during solidification of an Al–Cu eutectic alloy: interrelation of thermal parameters, microstructure and hardness. *J Therm Anal Calorim.* 2019;137:983–96. <https://doi.org/10.1007/s10973-018-07992-x>.
25. Krol M, Snopinski P, Czech A. The phase transitions in selective laser-melted 18-Ni (300-grade) maraging steel. *J Therm Anal Calorim.* 2020. <https://doi.org/10.1007/s10973-020-09316-4>.
26. Chulkov AO, Sfarra S, Saeed N, Ibarra-Castanedo C, Gargiulo G, Steenackers G, Maldague XPV, Omar MA, Vavilov V. Evaluating quality of marquetries by applying active IR thermography and advanced signal processing. *J Therm Anal Calorim.* 2020. <https://doi.org/10.1007/s10973-020-09326-2>.

Publisher's Note Springer Nature remains neutral with regard to jurisdictional claims in published maps and institutional affiliations.